ACS APPLIED MATERIALS & INTERFACES

Research Article

www.acsami.org

1-D Structured Flexible Supercapacitor Electrodes with Prominent Electronic/Ionic Transport Capabilities

Ju Seong Kim,[†] Seong Sik Shin,[†] Hyun Soo Han,[‡] Lee Seul Oh,[§] Dong Hoe Kim,[†] Jae-Hun Kim,[¶] Kug Sun Hong,*[,†] and Jin Young Kim*[,§,⊥]

[†]Department of Materials Science and Engineering, Seoul National University, Seoul, 151-744, Korea

[‡]Research Institute of Advanced Materials, Seoul National University, Seoul, 151-744, Korea

[§]Photo-electronic Hybrid Research Center, Korea Institute of Science and Technology, Seoul 136-791, Korea

[⊥]Green School, Korea University, Seoul 136-701, Korea

[¶]School of Advanced Materials Engineering, Kookmin University, Seoul 136-702, Korea

Supporting Information

ABSTRACT: A highly efficient 1-D flexible supercapacitor with a stainless steel mesh (SSM) substrate is demonstrated. Indium tin oxide (ITO) nanowires are prepared on the surface of the stainless steel fiber (SSF), and MnO_2 shell layers are coated onto the ITO/SSM electrode by means of electrodeposition. The ITO NWs, which grow radially on the SSF, are single-crystalline and conductive enough for use as a current collector for MnO_2-based supercapacitors. A flake-shaped, nanoporous, and uniform MnO_2 shell layer with a thickness of ~130 nm and an average crystallite size of ~2 nm is obtained by electrodeposition at a constant voltage. The effect of the electrode geometry on the supercapacitor properties was investigated using electrochemical impedance spectroscopy, cyclic voltammetry, and a galvanostatic charge/discharge study. The electrodes with ITO NWs exhibit higher specific capacitance levels and good rate capability owing to the superior electronic/ionic transport capabilities resulting from the open pore structure. Moreover, the use of a porous mesh substrate (SSM) increases the specific capacitance to 667 F g^{-1} at 5 mV s^{-1}. In addition, the electrode with ITO NWs and the SSM shows very stable cycle performance (no decrease in the specific capacitance after 5000 cycles).

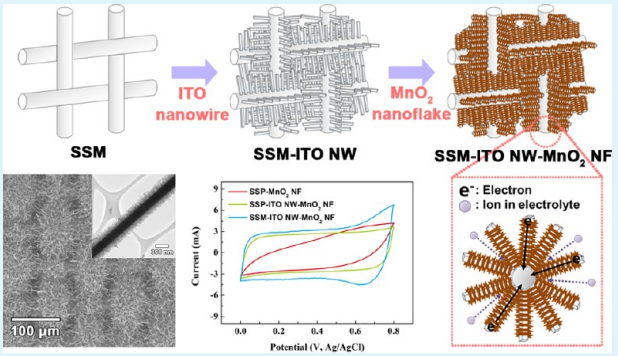

KEYWORDS: *ITO nanowire, MnO_2, supercapacitor, electron transport, ion transport*

INTRODUCTION

Due to the increasing demand for sustainable and renewable energy sources in electronic industries such as electric vehicles and portable electronics, environmentally friendly and flexible energy storage systems have attracted much research interest. Supercapacitors, also known as electrochemical capacitors or ultracapacitors, featuring high power densities, fast charge/discharge rates, and long cycle lifetimes, are among the most promising energy storage systems.[1−4] There are two types of supercapacitors depending on the charge/discharge mechanism on the electrode surface: electrical double-layer capacitors (EDLCs) using carbon materials[5−8] and pseudocapacitors based on transition-metal oxides or conducting polymers.[9−13] EDLCs store the charge electrostatically by the reversible adsorption of ions in an electrolyte on the surface of their electrode materials, exhibiting a high power density and low specific capacitances owing to their use of only the surface between the electrode and the electrolyte. In contrast to EDLCs, pseudocapacitors store the charge by means of a faradaic reaction between redox materials in a manner similar to that used in batteries, leading to high specific capacitances.[14,15]

Transient metal oxides (e.g., RuO_2, MnO_2, and NiO) with variable valence states have been studied widely due to high specific capacitance and energy density.[10,16−22] Among these candidates, MnO_2, which has a high theoretical specific capacitance value (1370 F g^{-1}), is regarded as the most attractive material due to its many advantages, such as its low cost and environmental friendliness.[19−22] However, the poor conductivity of MnO_2 (10^{-5}~10^{-6} S cm^{-1}) results in a low specific capacitance and insufficient rate capability.[23] To improve these electrochemical properties of MnO_2-based electrodes and use then in high-power applications, it is important to enhance the electron and ion transport properties. Extensive studies have focused on enhancing the electrochemical properties for supercapacitor electrodes using nanostructured materials.[24−30] Recently, hybrid structures composed of MnO_2 and highly conductive types of nanowires such as SnO_2,[31] Zn_2SnO_4,[32] indium tin oxide (ITO),[33] and Co_3O_4[34] to

Received: September 23, 2013
Accepted: December 17, 2013
Published: December 26, 2013

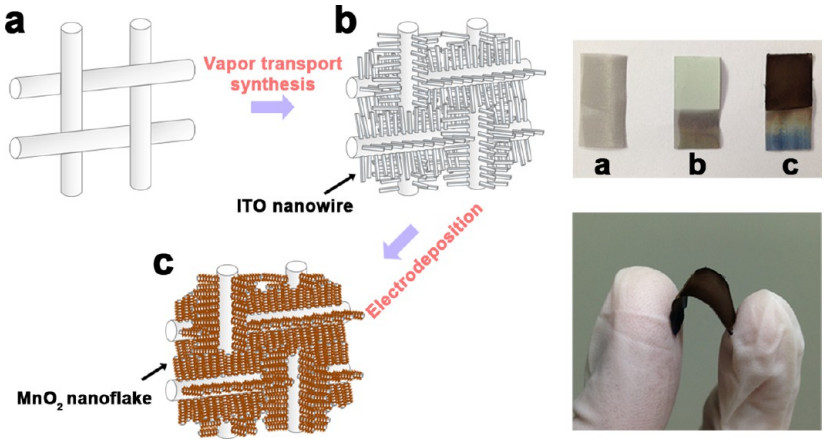

Figure 1. Schematic illustration of the SSM-ITO NW-MnO_2 NF fabrication process. (a) Prepared SSM substrate, (b) SSM-ITO NW electrode synthesized by the vapor transport method, and (c) a SSM-ITO NW-MnO_2 NF electrode deposited by potentiostatic electrodeposition. The upper inset shows optical images of the prepared electrodes and the lower inset shows the flexibility of the SSM-ITO NW-MnO_2 NF electrode.

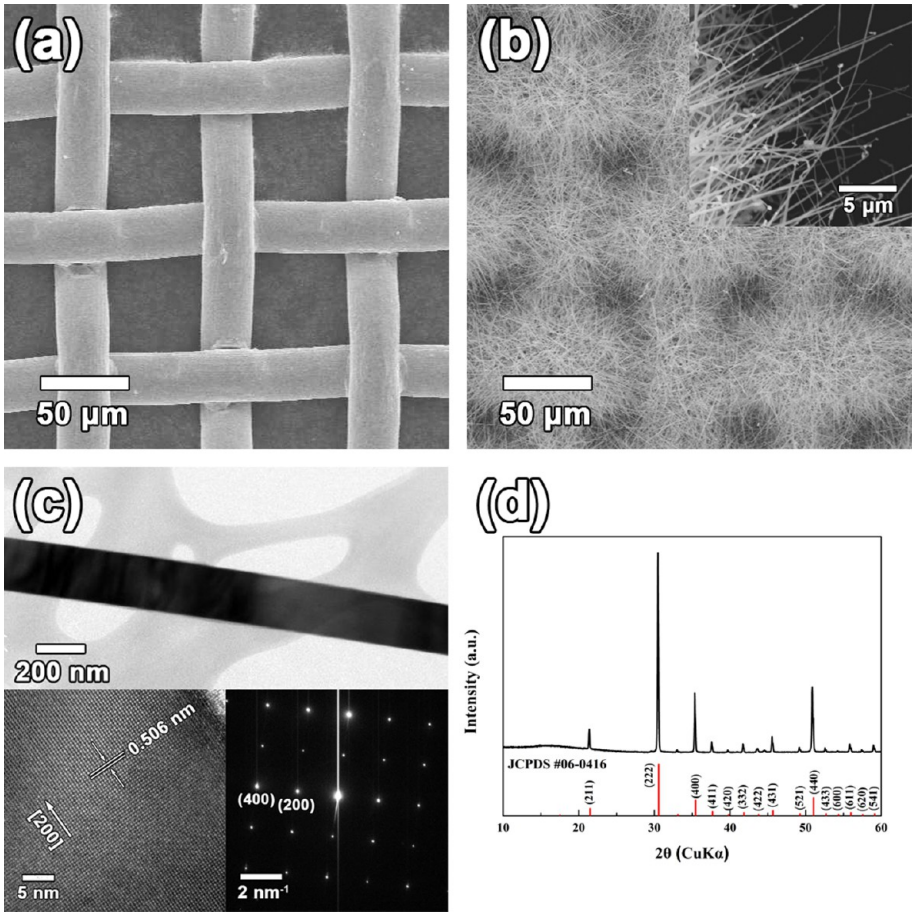

Figure 2. SEM images of (a) a SSM substrate and (b) a SSM-ITO NW electrode. The inset is a high-magnification image of a synthesized ITO NW. (c) TEM image of an individual ITO NW. Insets show a lattice fringe image and the SAED pattern of the ITO NW with a single-crystalline structure, which grew along the [200] direction. (d) XRD pattern of a SSM-ITO NW electrode.

enhance the electron transport properties have been reported. These materials have led to improvements in the specific capacitance and rate capability values. However, research with the goal of improving the electrochemical properties by controlling the ion transport properties in nanostructured materials remains insufficient.

In this study, we designed stainless steel mesh (SSM)-ITO nanowire (NW)-MnO_2 nanoflake (NF) electrodes as efficient supercapacitor electrodes and investigated their electrochemical properties. For comparison, stainless steel plate (SSP)-MnO_2 nanoflake (NF) and stainless steel plate (SSP)-ITO nanowire (NW)-MnO_2 nanoflake (NF) electrodes were also prepared. ITO NW, with its high conductivity, enhances the electron transport, and the open pore structure of the SSM substrate provides an ion diffusion channel which can decrease the degree of Warburg impedance. The specific capacitance of the

dx.doi.org/10.1021/am404132j | ACS Appl. Mater. Interfaces 2014, 6, 268−274

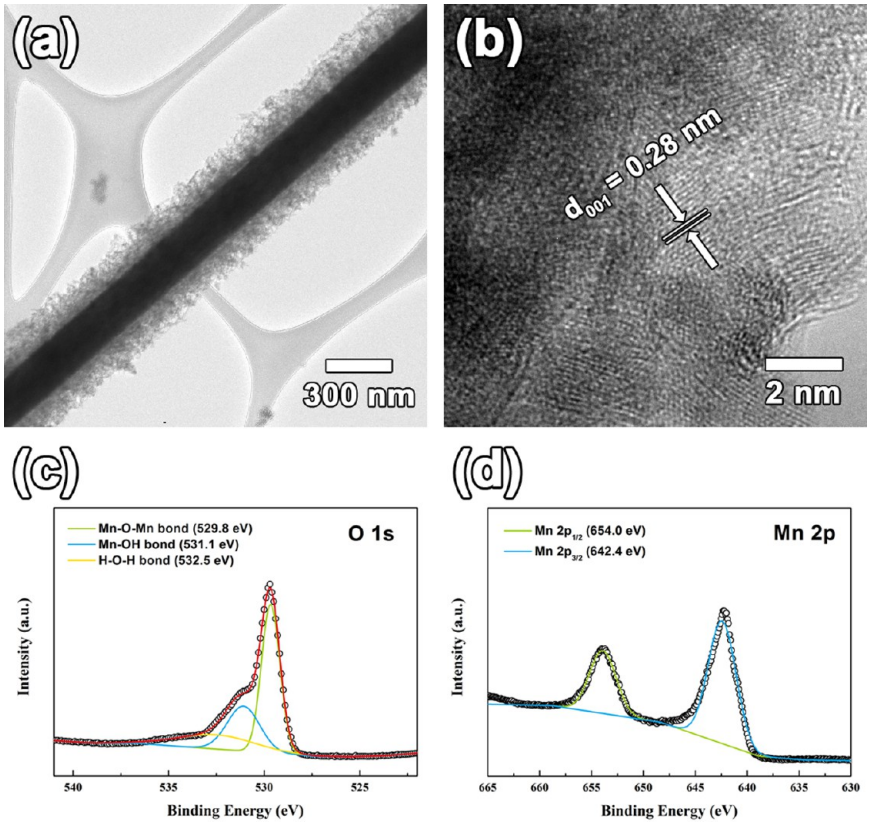

Figure 3. (a) Low-magnification image of deposited MnO_2 NF on an individual ITO NW and (b) lattice fringe image of MnO_2 NF showing its amorphous structure. (c) O 1s level spectrum of MnO_2 NF. The raw data is denoted by dots, which are deconvoluted into three peaks at 529.8 (Mn−O−Mn bond), 531.1 (Mn−OH bond), and 532.5 eV (H−O−H bond). (d) Mn 2p level spectrum of MnO_2 NF. The raw data is denoted by dots, which are deconvoluted into two peaks at 654.0 (Mn $2p_{1/2}$) and 642.4 eV (Mn $2p_{3/2}$).

SSM-ITO NW-MnO_2 electrode (667 F g^{-1} at scan rate of 5 mV s^{-1}) was higher than that of a SSP-ITO NW-MnO_2 electrode (413 F g^{-1}) and of a SSP-MnO_2 NF electrode (282 F g^{-1}). Moreover, the SSM-ITO NW-MnO_2 electrode can be used for flexible supercapacitors due to the flexibility of the SSM substrate, as shown in the lower inset of Figure 1. These results demonstrate that the SSM-ITO NW-MnO_2 NF electrode is a promising electrode that offers efficient electron transport and good ion transport properties.

METHODS

Synthesis of the SSM-ITO NW-MnO_2 NF Electrode. The fabrication procedure of the SSM-ITO NW-MnO_2 NFs electrode is schematically illustrated in Figure 1. First, the vapor transport method (VTM) was used to synthesize the ITO NWs on SSM substrates. A mixture composed of high-purity In (99.99%) and Sn (99.9%) metal powders with an atomic ratio of 9:3 was used as the VTM source. The mixture was loaded into a quartz boat and placed at the center of a quartz tube in a vacuum-tube furnace. The substrate was then placed at the end of the quartz tube. The temperature and atmospheric pressure of the vacuum-tube furnace for the synthesis of the ITO NWs were 800 °C and 1.5 mTorr, respectively. These values were maintained for 10 min. Oxygen gas for the formation of the ITO NWs was introduced into the quartz tube at a flow rate of 6.5 sccm for 30 min, and the furnace was cooled to room temperature at the same oxygen pressure. Second, MnO_2 NFs were deposited uniformly onto the ITO NWs by potentiostatic electrodeposition. The deposition process was performed in a three-electrode configuration with the prepared substrates as the working electrode, a Pt plate as the counter electrode and an Ag/AgCl electrode as the reference electrode. The MnO_2 NFs were potentiostatically deposited in a mixed solution composed of 0.5 M $Mn(CH_3COO)_2$ and 0.5 M CH_3COONa at voltage of 0.45 V with a deposition charge of 0.2 C cm^{-2}. The thickness of the MnO_2 NFs was controlled by varying the total amount of the charge during the electrodeposition process. After this process, the substrates were washed with distilled water several times and annealed at 350 °C for 1 h in air. The electrodeposition of all samples (SSM-ITO NW-MnO_2 NF, SSP-ITO NW-MnO_2 NF, and SSP-MnO_2 NF) proceeded under the same conditions. Optical images of the (a) SSM, (b) SSM-ITO NW, and (c) SSM-ITO NW-MnO_2 NF electrodes are shown in the upper inset of Figure 1. The size of the active area in all cases is 1 cm^2 (1 cm × 1 cm).

Characterization. The morphologies and lattice images of the SSM-ITO NW-MnO_2 NFs were investigated using a field emission scanning electron microscope (FESEM, SU-70, JEOL) and a high-resolution transmission electron microscope (HRTEM, JEM-3000F, JEOL). X-ray diffractometry (XRD, New D8 advance, Bruker) with Cu Kα radiation was used to analyze the crystalline structure of the ITO NW. An analysis of the chemical composition of the MnO_2 NF was done by means of X-ray photoelectron spectroscopy (XPS, Al Kα X-ray source, Sigma Probe) during which the binding energy was calculated with contaminated carbon (C 1s peak at 284.5 eV). The electrochemical properties of the prepared electrodes were measured with cyclic voltammetry (CV) and by assessing the galvanostatic charge/discharge rates using a three-electrode configuration with an electrochemical potentiostat (CHI 608C, CH Instruments) in a 0.5 M Na_2SO_4 aqueous solution in a potential range of 0 to 0.8 V. Electrochemical impedance spectroscopy (EIS) was measured in the frequency range of 0.1 to 100 000 Hz at 0 V with an amplitude of 5 mV. A microbalance (ME5, Sartorius) with an accuracy of 0.001 mg was used to measure the mass of the active material.

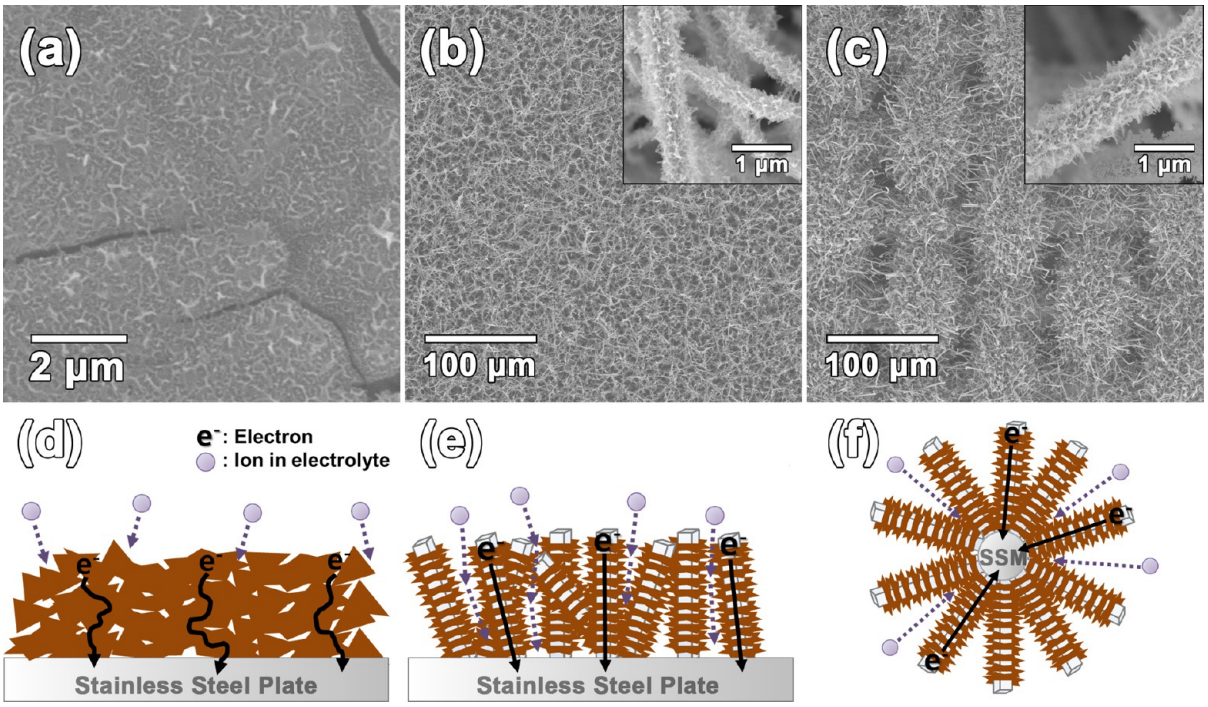

Figure 4. SEM images of (a) the SSP-MnO_2 NF electrode, (b) the SSP-ITO NW-MnO_2 NF electrode, and (c) the SSM-ITO NW-MnO_2 NF electrode. Insets show high-magnification images of the MnO_2-coated ITO NW sample, and the (d, e, f) lower images are schematic illustrations of the electrode structures of the corresponding SEM images.

RESULTS AND DISCUSSION

Synthesis of SSM-ITO NW-MnO_2 NF Electrode. The morphology and crystal structure of the SSM-ITO NW prepared by the VTM method is shown in Figure 2. Figure 2a shows a scanning electron microscope (SEM) image of a bare-SSM sample (325 mesh). The flexible conductive substrate consists of stainless steel fibers with a diameter of 28 μm, with an average pore size of approximately 50 μm. Figure 2b displays a SEM image of the SSM substrate after the VTM growth of ITO NWs, which will serve as a backbone for the MnO_2 NFs. It was found from the SEM images that ITO NWs with lengths ranging from 10 to 40 μm grew vertically on the surface of the stainless steel fiber. The structural properties of the ITO NWs were further investigated by means of transmison electron microscopy (TEM), as shown in Figure 2c. The diameter of a single ITO NW ranges from 100 to 200 nm, leading to an aspect ratio higher than 100. A high-resolution image (lower left inset in Figure 2c) exhibits the clear lattice fringe of the (200) planes with a spacing of 5.06 Å, indicating that the ITO NWs grow along the [200] direction. The corresponding selected-area electron diffraction (SAED) pattern (lower right inset of Figure 2c) shows a clear spot pattern, indicating that the ITO NW is a single-crystalline sample with a cubic structure. Figure 2d shows the X-ray diffraction (XRD) pattern of ITO NWs grown on a SSM substrate, where the diffraction pattern perfectly matches the predicted diffraction peaks of the cubic In_2O_3 structure (JCPDS #06-0416). In general, the XRD patterns of vertically aligned single-crystalline ITO NWs exhibit strong (400) diffraction peaks due to the preferential growth along the [200] direction. In our case, however, the relative intensity of the (400) diffraction peak is very close to that on the JCPDS card (i.e., polycrystalline ITO), because ITO NWs grow radially on the cylindrical surface of the stainless steel fiber. It should be noted that the ITO NW has very low electrical resistivity (4.7×10^{-4} Ω cm^{-1}).[35] Owing to the high conductivity of the ITO NW, it can function not only as a structural scaffold but also as a current collector for a MnO_2 NF capacitor. The high conductivity of ITO NWs is also very important for the successful formation of the MnO_2 layer, as it serves as an electrode during the electrodeposition process.

Figure 3 shows the morphology and XPS spectra of a MnO_2 NF (or the shell layer) electrodeposited on the surface of an ITO NW. A low-magnification TEM image (Figure 3a) reveals that the MnO_2 NF with an average thickness of 130 nm uniformly covers the ITO NW, and a high-resolution image (Figure 3b) further shows that the MnO_2 NF layer consists of very fine crystallites with a diameter of approximately 2 nm dispersed in an amorphous matrix. In spite of the small size of the MnO_2 crystallites, clear lattice fringes with a interplanar spacing of 0.28 nm can be observed, corresponding to the (001) plane of α-MnO_2. Figure 3c,d displays the XPS spectra of the O 1s and Mn 2p samples, respectively. A full-range XPS spectrum is shown in the Supporting Information (Figure S1). The O 1s spectrum can be decomposed into three separate peaks after a Gaussian multipeak-deconvolution process. The peaks at 529.8, 531.1, and 532.5 eV can be assigned to the Mn−O−Mn bond in an oxide form, to the Mn−OH bond in a hydroxide form, and to the H−O−H bond in water, respectively, in good agreement with previous reports.[36,37] The strong Mn−O−Mn peak with a smaller Mn−OH peak and a traceable H−O−H peak indicate that the MnO_2 NF mainly consists of Mn-oxide with a small amount of the hydroxide form and adsorbed water molecules. The Mn 2p spectrum is composed of two peaks at 642.4 and 654.0 eV with a difference of 11.6 eV, which is consistent with the spin-energy separation energy in the literature.[19,32,36,37]

dx.doi.org/10.1021/am404132j | ACS Appl. Mater. Interfaces 2014, 6, 268−274

SEM images of SSP-MnO_2 NF, SSP-ITO NW-MnO_2 NF, and SSM-ITO NW-MnO_2 NF electrodes are shown in Figure 4, where the lower images schematically illustrate their structures. In the case of the SSP-MnO_2 NF electrode (Figure 4a), the planar SSP substrate is fully covered by the thick MnO_2 layer. During the capacitive reaction, therefore, the electrons should be transported through the MnO_2 layer before being collected by the SSP substrate. Poor electrical conductivity of the MnO_2 layer hinders charge/discharge reaction, especially at fast reaction. Furthermore, the Na^+ or H^+ ions in the electrolyte cannot penetrate the MnO_2 layer, resulting in a decrease of the activated MnO_2 during the charge/discharge reaction. On the other hand, in the electrodes with ITO NWs (Figure 4b,c), the electrons only need to travel across the thin MnO_2 layer (~130 nm) before being collected by the conductive ITO NWs, indicating that electrical conduction during the capacitive reaction is not a problem for either the SSP-ITO NW-MnO_2 NF electrode or the SSM-ITO NW-MnO_2 NF electrode. Although these two electrodes have similar active layer (i.e., MnO_2) morphologies, their pore structures are quite different. The ITO NWs grown on the planar substrate (i.e., SSP-ITO NW-MnO_2 NF in Figure 4b) cross each other, resulting in a complicated and tortuous pore structure. On the other hand, the ITO NWs grown on the fibular substrate (i.e., SSM-ITO NW-MnO_2 NF in Figure 4c) do not cross as much as their planar counterparts due to the curvature of the substrate, leading to a relatively open pore structure. Given that the open pore structure aids ionic transport in the electrolyte, the SSM-ITO NW-MnO_2 NF electrode results in the most efficient supercapacitor structure among three electrodes.

Electrochemical Properties and Performance Levels. Electrochemical impedance spectroscopy (EIS) was performed on the electrodes. Figure 5 shows Nyquist plots of SSP-MnO_2, SSP-ITO NW-MnO_2 NF, and SSM-ITO NW-MnO_2 NF electrodes, where the insets show the equivalent circuit (upper inset; Randles equivalent circuit) and a magnified view of the high-frequency region (lower inset). The equivalent series resistance (ESR) R_s value is usually a combination of the ionic resistance of the electrolyte, the substrate resistance, and the contact resistance with the current collector. The R_s values of the SSP-MnO_2 NF, SSP-ITO NW-MnO_2 NF, and SSM-ITO NW-MnO_2 NF electrodes obtained from the x-intercepts of magnified Nyquist plots are similar, indicating that the resistance was not affected by the incorporation of ITO NWs. On the other hand, only SSP-MnO_2 NF exhibits an apparent semicircle with a high R_{ct} value, which can be derived from the diameter of the semicircle. The charge-transfer resistance is related to the charge-transfer barriers, including the "electron transfer" between the current collector and the active material and the "ion transfer" between the active material and the electrolyte. Therefore, the relatively low R_{ct} values of the electrodes with ITO NW can be attributed to the geometry of each electrode.

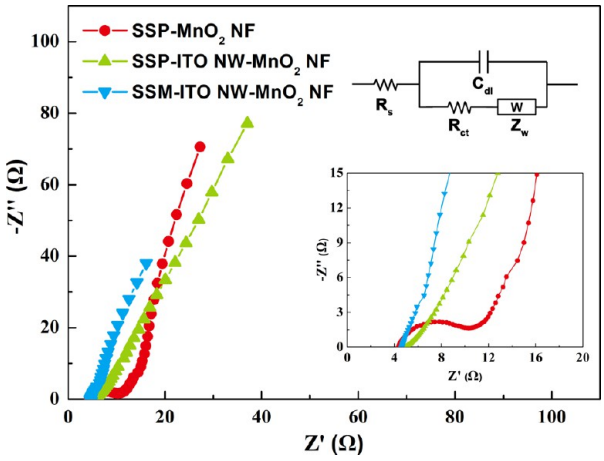

Figure 5. Impedance spectra of three prepared types of electrodes. The upper inset shows the equivalent circuit diagram and the lower inset shows the impedance spectra in the high-frequency region.

Figures 6a and S2a,b, Supporting Information, show the cyclic voltammetry (CV) curves of SSM-ITO NW-MnO_2 NF, SSP-MnO_2 NF, and SSP-ITO NW-MnO_2 NF electrodes at various scan rates (5, 10, 20, 50, and 100 mV s^{-1}) in the potential range of 0−0.8 V. Their specific capacitance values are plotted as a function of the scan rate. The charge/discharge processes or the capacitive reaction during the CV measurement in the aqueous Na_2SO_4 electrolyte can be expressed by the following faradaic reaction:[36]

$$MnO_2 + C^+ + e^- \leftrightarrow MnOOC$$

$$C^+ = H^+ \text{or } Na^+$$

At low scan rates (i.e., 5, 10 mV s^{-1}), the CV curves of all samples exhibit a nearly rectangular shape, indicating that the redox reaction is fast enough for all electrodes at the measured scan rate. However, the shape of the CV curves of the SSP-MnO_2 NF (Figure S2a, Supporting Information) sample changes at higher scan rates, indicative of the slower reaction kinetics at the relatively high scan rate. On the other hand, the shape of the CV curves for the electrodes with ITO NWs does not change significantly, even at a very high scan rate of 100 mV s^{-1} (Figure S2b, Supporting Information, and Figure 6a), suggesting that the presence of the ITO NWs actually facilitates electronic and ionic transport and thus improves the kinetics of the capacitive reaction. These findings are also in good agreement with the EIS results. Figure 6b compares the specific capacitance of the three electrodes with the increasing scan rate, as calculated from the CV curves using the following equation:

$$C = \int_{V_1}^{V_2} i(V)\, dV / m\upsilon(V_2 - V_1) \quad (1)$$

Here, C is the specific capacitance, V_2 and V_1 are the upper and lower ends of the potential sweep during the CV measurements, $i(V)$ is the instantaneous current, $\int_{V_1}^{V_2} i(V)\, dV$ is the total amount of the discharged charge, m is the mass of the MnO_2, and υ is the scan rate. In the entire scan rate range, the SSM-ITO NW-MnO_2 NF exhibits the highest specific capacitance and the SSP-MnO_2 NF shows the lowest specific capacitance. At 5 mV s^{-1}, for example, the specific capacitances of the SSM-ITO NW-MnO_2 NF, SSP-ITO NW-MnO_2 NF, and SSP-MnO_2 NF samples were 667, 413, and 282 F g^{-1}, respectively. The higher specific capacitance values of the electrodes with the ITO NWs as compared to the SSP-MnO_2 NF can be ascribed to the high active surface caused by the incorporation of ITO NWs and the thinner MnO_2, leading to more efficient utilization of the MnO_2 during the capacitive reaction. The incorporation of a mesh substrate (i.e., SSM-ITO NW-MnO_2 NF) as opposed to a planar substrate increases the specific capacitance further owing to high surface area of the mesh

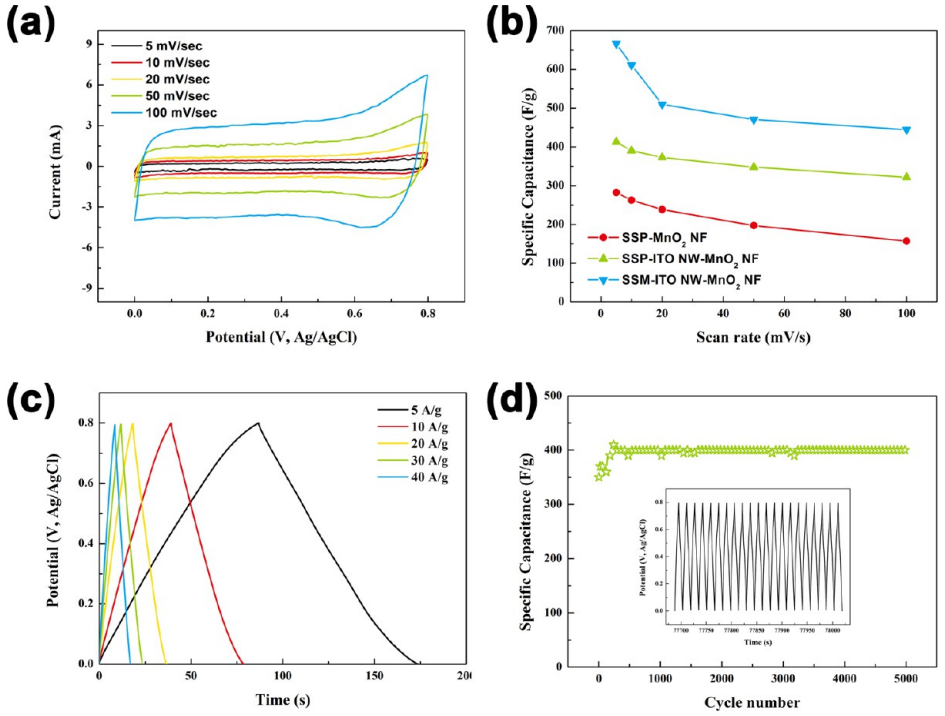

Figure 6. Cyclic voltammetry curves of (a) SSM-ITO NW-MnO_2 NF at different scan rates. (b) Variation of the specific capacitances of prepared electrodes as a function of the scan rate. (c) Galvanostatic charge/discharge curves at different current densities. (d) Cycle performance of SSM-ITO NW-MnO_2 NF electrode at a constant current density 40 A/g (5000 cycles). The inset shows the galvanostatic charge/discharge curves of the last 20 cycles.

structure and/or the easier penetration of the electrolyte. Such an enhancement becomes more apparent at lower scan rates because the contribution to the specific capacitance by the bulkier cations (e.g., Na^+ as opposed to H^+) is likely to increase at a lower scan rate. The specific capacitances of all samples decrease with an increase in the scan rate, reaching 445, 322, and 157 F g^{-1} at 100 mV s^{-1} in the SSM-ITO NW-MnO_2 NF, SSP-ITO NW-MnO_2 NF, and SSP-MnO_2 NF cases, featuring decrements of 33.3%, 22.1%, and 44.3%, respectively. It is noteworthy that the electrodes with ITO NWs show better rate capability levels compared to the SSP-MnO_2 samples; this can be attributed to the enhanced charge transport during the charge/discharge processes. Specific capacitance values calculated from the galvanostatic charge/discharge (GV) curves also showed similar dependence on the electrode geometry (Figure S3 in the Supporting Information).

Figure 6c shows the GV curves of the SSM-ITO NW-MnO_2 NF sample at various current densities (5, 10, 20, 30, and 40 A g^{-1}). The curves are highly symmetric regardless of the current density, indicative of the good capacitive characteristics and superior reversible redox reaction. A test of the cycling lifetime for more than 5000 cycles for the SSM-ITO NW-MnO_2 NF was performed using GV measurements at a high current density of 40 A g^{-1} with a potential window ranging from 0 to 0.8 V. Figure 6d displays the variation of the specific capacitance as a function of the cycle number, where the inset shows the GV curves of the last 20 cycles. The capacitance of the SSM-ITO MnO_2 electrode increases slightly during the cycling process, most likely due to the slow infiltration of the electrolyte into the nanopores within the MnO_2 active material layer during the initial cycling process.[38] The specific capacitance after 5000 cycles is 400 F g^{-1}, which is 14% higher than the initial value and 3% lower than the maximum value. In addition, the GV curves during the last 20 cycles retain their original symmetric shape, revealing the good long-term cycle stability of the SSM-ITO NW-MnO_2 NF.

CONCLUSION

In summary, a highly efficient 1-D flexible supercapacitor based on a stainless steel mesh (SSM) and ITO NWs was demonstrated. Highly conductive ITO NWs were grown radially on the surface of a stainless steel plate (SSP) of fiber (stainless steel fiber (SSF)) via a vapor transport method, and a MnO_2 shell layer (i.e., an active material) was deposited on the surfaces of bare-SSP or ITO NWs by means of electrodeposition. The supercapacitive properties of the electrodes with different geometries were investigated in terms of the structure−property relationship. The electrodes with ITO NWs exhibit higher specific capacitances and superior rate capability levels compared to those with a bare-SSP substrate owing to their superior electronic (by ITO NWs) and ionic (by open pore structure) transport capabilities, in good agreement with the EIS analysis. The use of SSM instead of a planar substrate (i.e., SSP) increases the specific capacitance further to 667 F g^{-1} at 5 mV s^{-1}. In addition, the best sample shows very good cycle stability, exhibiting essentially no decrease after 5000 cycles. The electrode geometry (i.e., SSM-ITO NW-MnO_2 NF) and the prominent supercapacitive behavior reported in this study should provide a rational for continuing improvements to the performance of highly efficient supercapacitors through the proper selection of the materials and the creation of feasible electrode geometry designs.

dx.doi.org/10.1021/am404132j | ACS Appl. Mater. Interfaces 2014, 6, 268−274

■ ASSOCIATED CONTENT

Supporting Information

Additional figures (XPS, cyclic voltammetry, galvanostatic charge/discharge curves, and rate capability). This information is available free of charge via the Internet at http://pubs.acs.org/.

■ AUTHOR INFORMATION

Corresponding Authors

*E-mail: kimjy@kist.re.kr.

*E-mail: kshongss@plaza.snu.ac.kr.

Notes

The authors declare no competing financial interest.

■ ACKNOWLEDGMENTS

This work was supported by the Global Frontier R&D Program of the Center for Multiscale Energy Systems funded by the National Research Foundation under the Ministry of Education, Science and Technology of Korea (2013-052268). The work done at KIST was supported by the KIST internal fund, the New & Renewable Energy Technology Development Program of the Korea Institute of Energy Technology Evaluation and Planning (KETEP) funded by the Ministry of Trade, Industry & Energy (No. 20113020010040), the Nano-Material Technology Development Program through the National Research Foundation of Korea (NRF) funded by the Ministry of Science, ICT & Future Planning (2012M3A7B4049989), and the "National Agenda Project" program of the Korea Research Council of Fundamental Science & Technology (KRCF). The work done at Green School was supported by a National Research Foundation of Korea grant funded by the Korean Government (MSIP) (2013, University-Institute Cooperation Program).

■ REFERENCES

(1) Simon, P.; Gogotsi, Y. *Nat. Mater.* **2008**, *7*, 845−854.

(2) Miller, J. R.; Simon, P. *Science* **2008**, *321*, 651−652.

(3) Chmiola, J.; Largeot, C.; Taberna, P.-L.; Simon, P.; Gogotsi, Y. *Science* **2010**, *328*, 480−483.

(4) Winter, M.; Brodd, R. J. *Chem. Rev.* **2004**, *104*, 4245−4270.

(5) Frackowiak, E.; Beguin, F. *Carbon* **2001**, *39*, 937−950.

(6) Stoller, M. D.; Park, S.; Zhu, Y.; An, J.; Ruoff, R. S. *Nano Lett.* **2008**, *8*, 3498−3502.

(7) Liu, C.; Yu, Z.; Neff, D.; Zhamu, A.; Jang, B. Z. *Nano Lett.* **2010**, *10*, 4863−4868.

(8) Xie, K.; Qin, X.; Wang, X.; Wang, Y.; Tao, H.; Wu, Q.; Yang, L.; Hu, Z. *Adv. Mater.* **2012**, *24*, 347−352.

(9) Liu, J.; Cheng, C.; Zhou, W.; Li, H.; Fan, H. J. *Chem. Commun.* **2011**, *47*, 3436−3438.

(10) Kim, J. Y.; Lee, S. H.; Yan, Y.; Oh, J.; Zhu, K. *RSC Adv.* **2012**, *2*, 8281−8285.

(11) Xia, X.; Tu, J.; Zhang, Y.; Wang, X.; Gu, C.; Zhao, X.-b.; Fan, H. J. *ACS Nano* **2012**, *6*, 5531−5538.

(12) Arbizzani, C.; Mastragostino, M.; Meneghello, L. *Electrochim. Acta* **1996**, *41*, 21−26.

(13) Snook, G. A.; Kao, P.; Best, A. S. *J. Power Sources* **2011**, *196*, 1−12.

(14) Conway, B.; Birss, V.; Wojtowicz, J. *J. Power Sources* **1997**, *66*, 1−14.

(15) Wang, G.; Zhang, L.; Zhang, J. *Chem. Soc. Rev.* **2012**, *41*, 797−828.

(16) Hu, C.-C.; Chang, K.-H.; Lin, M.-C.; Wu, Y.-T. *Nano Lett.* **2006**, *6*, 2690−2695.

(17) Zang, J.; Bao, S.-J.; Li, C. M.; Bian, H.; Cui, X.; Bao, Q.; Sun, C. Q.; Guo, J.; Lian, K. *J. Phys. Chem. C* **2008**, *112*, 14843−14847.

(18) Kim, J.-H.; Zhu, K.; Yan, Y.; Perkins, C. L.; Frank, A. J. *Nano Lett.* **2010**, *10*, 4099−4104.

(19) Liu, J.; Jiang, J.; Bosman, M.; Fan, H. J. *J. Mater. Chem.* **2012**, *22*, 2419−2426.

(20) Xu, C.; Zhao, Y.; Yang, G.; Li, F.; Li, H. *Chem. Commun.* **2009**, 7575−7577.

(21) Chen, W.; Fan, Z.; Gu, L.; Bao, X.; Wang, C. *Chem. Commun.* **2010**, *46*, 3905−3907.

(22) Lu, X.; Zheng, D.; Zhai, T.; Liu, Z.; Huang, Y.; Xie, S.; Tong, Y. *Energy Environ. Sci.* **2011**, *4*, 2915−2921.

(23) Desilvestro, J.; Haas, O. *J. Electrochem. Soc.* **1990**, *137*, 5C−22C.

(24) Hou, Y.; Cheng, Y.; Hobson, T.; Liu, J. *Nano Lett.* **2010**, *10*, 2727−2733.

(25) Liu, J.; Essner, J.; Li, J. *Chem. Mater.* **2010**, *22*, 5022−5030.

(26) Yu, G.; Hu, L.; Liu, N.; Wang, H.; Vosgueritchian, M.; Yang, Y.; Cui, Y.; Bao, Z. *Nano Lett.* **2011**, *11*, 4438−4442.

(27) Chen, W.; Rakhi, R.; Hu, L.; Xie, X.; Cui, Y.; Alshareef, H. *Nano Lett.* **2011**, *11*, 5165−5172.

(28) Yu, G.; Hu, L.; Vosgueritchian, M.; Wang, H.; Xie, X.; McDonough, J. R.; Cui, X.; Cui, Y.; Bao, Z. *Nano Lett.* **2011**, *11*, 2905−2911.

(29) Yu, L.; Zhang, G.; Yuan, C.; Lou, X. W. D. *Chem. Commun.* **2013**, *49*, 137−139.

(30) Lu, X.; Zhai, T.; Zhang, X.; Shen, Y.; Yuan, L.; Hu, B.; Gong, L.; Chen, J.; Gao, Y.; Zhou, J. *Adv. Mater.* **2012**, *24*, 938−944.

(31) Yan, J.; Khoo, E.; Sumboja, A.; Lee, P. S. *ACS Nano* **2010**, *4*, 4247−4255.

(32) Bao, L.; Zang, J.; Li, X. *Nano Lett.* **2011**, *11*, 1215−1220.

(33) Dam, D. T.; Lee, J.-M. *Nano Energy* **2013**, *2*, 933−942.

(34) Liu, J.; Jiang, J.; Cheng, C.; Li, H.; Zhang, J.; Gong, H.; Fan, H. J. *Adv. Mater.* **2011**, *23*, 2076−2081.

(35) Noh, J. H.; Han, H. S.; Lee, S.; Kim, J. Y.; Hong, K. S.; Han, G. S.; Shin, H.; Jung, H. S. *Adv. Energy Mater.* **2011**, *1*, 829−835.

(36) Toupin, M.; Brousse, T.; Bélanger, D. *Chem. Mater.* **2004**, *16*, 3184−3190.

(37) Rakhi, R. B.; Chen, W.; Cha, D.; Alshareef, H. *Adv. Energy Mater.* **2012**, *2*, 381−389.

(38) Kim, J.-H.; Kang, S. H.; Zhu, K.; Kim, J. Y.; Neale, N. R.; Frank, A. J. *Chem. Commun.* **2011**, *47*, 5214−5216.